

# A multi-field coupled FEM model for one-step-forming process of spark plasma sintering considering local densification of powder material

Yi Song · Yuanyuan Li · Zhaoyao Zhou ·  
Yangen Lai · Yongquan Ye

Received: 22 December 2010 / Accepted: 30 March 2011 / Published online: 12 April 2011  
© Springer Science+Business Media, LLC 2011

**Abstract** A mechanical constitutive model of powder material is introduced to a fully coupled thermal–electric–mechanical finite element model to simulate the one-step-forming spark plasma sintering (SPS) process of metal powders. The effects of displacement field and local density distribution on sintering are considered in this article, which are generally neglected in the existing SPS models. The mechanical, thermal, and electrical parameters of powders are assumed as functions of local relative density and temperature. The simulated varying displacement field remodels the distributions of temperature and electric potential by changing the contact thermoelectric resistances. For the 20, 40, and 60 MPa external pressures, the simulation indicates that the sintering temperature and the temperature gradient within powders are decreased by enhancing the external pressure, and the comprehensive effect of stress promotes the densification of the colder regions. Thus, the interrelationship between the temperature gradient and the intrinsic stress distribution plays an important role in the densification mechanism of SPS powders.

## Introduction

Spark plasma sintering (SPS) is known as a single step processing technique, which combines the electric field sintering technique and the uniaxial pressing forming technique. Some important technological benefits of SPS, such as higher heating rates, fewer processing steps,

elimination of the need for sintering aids, and near net shape capacity, facilitate controlling the grain growth and improving the mechanical, chemical, and physical properties of powder materials [1, 2]. These advantages over other conventional methods of powder consolidation give rise to the worldwide popularity of SPS. However, the sintering mechanism of SPS is still unclear because of some unexplainable microscopic and macroscopic phenomena in the coupled multi-physical fields, as well as the difficulty in measuring the interior temperature of samples [3, 4].

Finite element method (FEM) is an effective analysis approach which is commonly applied in the mechanism researches of SPS. FEM material models and thermoelectric boundaries are established to simulate the coupled effects of the interior temperature field, electrical field, and outside pressure. Some SPS macroscopic models [5–8] which address the thermal–electrical coupling, can describe the complex features of temperature field and electric field precisely and explain the material heterogeneity produced in the SPS process to a certain extent. Wang et al. [9] firstly presented a coupled thermal–electrical–mechanical FEM model to focus on the influences of various material properties and control parameters on temperature and stress distributions. Nevertheless, like many others, this model was limited to the fully dense solid compacts and the simulative results of stress gradients were obtained from the linear elastic continuum material model without considering the densification process, which is not entirely consistent with most of the one-step-forming SPS processes.

So far, for the powder material, there are few SPS FEM analyses considering the evolution of the local density distribution and its effect on material properties. McWilliams and Zavaliongos [10] applied a creep constitutive

Y. Song (✉) · Y. Li · Z. Zhou · Y. Lai · Y. Ye  
School of Mechanical and Automotive Engineering, South China  
University of Technology, Guangzhou 510640, China  
e-mail: songyi0591@gmail.com

equation to simulate the sintering of a conductive rectangular compact with an initial density variation. This study utilized two finite element modules including a thermal-electrical simulation part and a thermal-displacement simulation part, and some interesting results were presented. But it was not for the usual SPS processes. Moreover, only the thermal and electrical conductivities were discussed as the density-dependent material properties, and the stress distribution was neglected.

The purpose of this study is to present a novel FEM model which is suitable for the one-step-forming SPS process. This model can predict the influence of the densification process on contact thermoelectric conduction and the interactions among the local density distribution, stress distribution and temperature gradient. It is useful for understanding the SPS mechanism of the materials sensitive to the variation of pressure and local temperature. This study is based on a precondition that powders are not precompressed into a nearly dense compact and there is a relatively low initial density before sintering. A kinetics constitutive model of powders is integrated into a fully coupled thermal-electrical-mechanical simulation procedure. The effects of the local densification behavior on material properties and contact thermoelectric resistances are taken into account for different pressures. The FEM calculations are derived from the user-subroutines of Marc and the simulations are compared with experiments.

## Experimental procedure

In order to validate the simulation, all experiments were conducted in vacuum using a commercial SPS sintering device (SPS-825, Japan). The 20 g iron powder particles with a mean particle size of 5  $\mu\text{m}$  were filled in a silicon-nitride die without any lubricants and additives. All samples had been pressed gently to the same initial relative density of 55.8% before the current was applied. The dimensions and positions of the SPS setup are shown in Fig. 1. A thermocouple was placed in a hole drilled in the silicon-nitride die (i.e., the position A marked in Fig. 1) for the temperature measurement. The sintering process was in a temperature control mode, and the heating rate was maintained at 50  $^{\circ}\text{C}/\text{min}$  by means of controlling the closed current loop feedback until the measured temperature reached 700  $^{\circ}\text{C}$ . Simultaneously, three different external unidirectional loads were applied to the top graphite spacer in the electrifying process, which were, respectively, equivalent to 20, 40, and 60 MPa nominal pressures on the sample and were removed rapidly at the moment of the power shutdown. The on-line data of displacement, voltage, current, and temperature were recorded as history profiles.

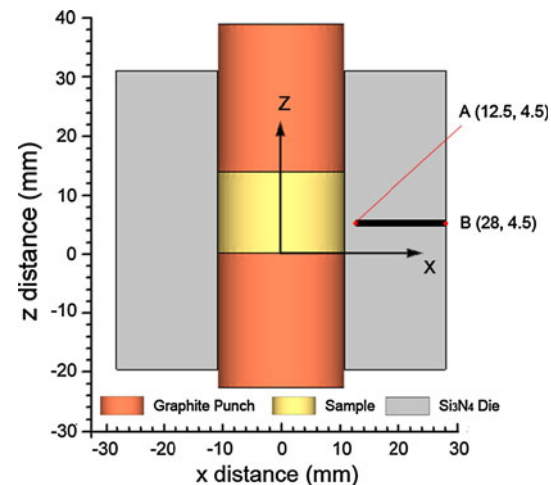


**Fig. 1** Dimensions and positions of the punch/die/sample setup. Point A ( $x = 12.5$  mm,  $z = 4.5$  mm) and point B ( $x = 28$  mm,  $z = 4.5$  mm) present the position where the thermocouple is placed

It is necessary to mention that the choice of the silicon-nitride die rather than the general graphite die is made for the purpose of an intentional big temperature gradient in the specimen, which helps to exhibit the effects of the densification process and stress on temperature field more intuitively and illustrate the necessity of this new model more effectively.

## FEM theoretical model

### Scheme of SPS multi-field coupling modeling

For the SPS process of powder material, the generation of Joule heat inside the specimen is always accompanied by a remarkable densification course. It is unadvisable to consider these two closely interrelated physical phenomena separately for an accurate FEM analysis, because in addition to the influences of temperature gradient on material properties and structural deformation, the structural deformation also reveals a back action on distributions of temperature field and electrical field through changing the boundaries of heat- and electrical-fluxes. And the heat transfer, mainly in the form of heat conduction, is susceptible to the local relative density. Besides, the outer pressure as one of the densification driving forces has been demonstrated to be much more significant than expected [11]. So it is essential to build connection between thermodynamics and the thermal-electrical coupling theory.

With the commercial FEM package Marc, the Joule heating and thermal viscoplastic behaviors of powders are simulated in a multi-field coupling scheme which consists of a thermal-electrical coupling solution modulus and a thermal-mechanical coupling user-subroutines solution modulus. The updated-Lagrange framework is adopted to

solve the coupled governing equations. Temperature  $T$  and local relative density  $\rho_r$  are designated as two state variables in user subroutines. When the increment step  $t = n$ , the temperature increment  $\Delta T^n$  is calculated upon the convergence tolerance of temperature in the thermal-electrical coupling solution modulus, and then it is invoked in the thermal-mechanical coupling solution modulus where  $\Delta T^n$ ,  $T^{n-1}$  and  $\rho_r^{n-1}$  are used to calculate  $\rho_r^n$  upon the convergence tolerance of residual stress or displacement. The state variables are updated at the end of the increment step  $t = n$ , and extracted at the beginning of the next increment step  $t = n + 1$ . So they are the repeated transmission mediums between the alternant iterative processes of energy conservation equations and mechanical equilibrium equations in every increment step.

#### Coupled thermal-electrical model

The partial differential equations for the distributions of electric potential and temperature are based on Ohm's and Fourier's laws, which are given as Eqs. 1 and 2, respectively [2]:

$$\nabla \cdot \vec{J} = \nabla \cdot [R(T, \rho_r) \vec{E}] = \nabla \cdot [-R(T, \rho_r) \nabla U] = 0 \quad (1)$$

where  $\vec{J}$  and  $\vec{E}$  present the electric current intensity and the electric field intensity, respectively,  $R$  is the electric conductivity which is the function of temperature  $T$  and relative density  $\rho_r$ , and  $U$  is the electric potential.

$$\rho c_p(T, \rho_r) \frac{\partial T}{\partial t} - \nabla \cdot [K(T, \rho_r) \nabla T] = \dot{q}_e + \dot{q}_r + \dot{q}_{conv} + \dot{q}_c \quad (2)$$

In Eq. 2,  $\rho$  is the density,  $c_p$  the heat capacity,  $K$  the thermal conductivity,  $t$  the time.  $\dot{q}_e$  represents the generated Joule heat per unit volume according to Joule's law.  $\dot{q}_r$  and  $\dot{q}_{conv}$  are surface heat fluxes by radiation and convection, respectively. Because the experiments are conducted in vacuum, the heat loss by convection through the air is ignored.  $\dot{q}_c$  represents the thermoelectric effects at contact interfaces owing to the imperfect contact situations, and consists of two parts:  $\dot{q}_{tc}$  the heat transfer through the contact interfaces and  $\dot{q}_{ec}$  the Joule heating of the contact electric resistances, which can be written as follows:

$$\dot{q}_c = \dot{q}_{tc} + \dot{q}_{ec} \quad (3)$$

$$\dot{q}_{tc} = h_{c,j}(T_{1,j} - T_{2,j}), \quad \dot{q}_{ec} = \alpha_{c,j}(U_{1,j} - U_{2,j})^2 \quad (4)$$

where  $h_{c,j}$  and  $\alpha_{c,j}$  are heat transfer coefficient and electric conductance of the contact gap, respectively. The subscript  $j$  denotes the  $j$ th contact pair, and the 1 and 2 represent two contact bodies in per contact pair.

The material properties of powders should take into account the continuous variation of local relative density in

this SPS model. The temperature dependence [2, 12, 13] and the density dependence [10] of material properties have been discussed in other literatures. In fact, without a precompression before the SPS process, the powder specimen will transform from the nearly insulating loose mass to the conductive dense one after sintering. Meanwhile, the dramatical variation of temperature could affect the heat and electrical conducting properties significantly. Therefore, the effective thermal conductivity  $K$  [14] and electrical conductivity  $R$  [15] are assumed as the bivariate functions of temperature and the relative density:

$$K = K_s(T)(1.5\rho_r - 0.5) \quad (5)$$

$$R = R_s(T)\rho_r^{(1+\rho_m^{0.8})} \quad (6)$$

where,  $K_s(T)$  and  $R_s(T)$  are the thermal and electrical conductivity of the corresponding fully dense material at the temperature  $T$ , respectively.  $\rho_m$  is designated as the minimum relative density of the system, which can be equivalent to the initial relative density of powders (i.e., 0.558). In particular, Eq. 6 is applicable to the powder-sintered compacts. The main thermoelectric and mechanical material parameters used in the numerical modeling are listed in Appendix.

#### Mechanical constitutive model

Considering the influence of porosity and hydrostatic pressure of porous materials, one general form of the yield criterion is given as follows:

$$f = A \cdot J'_2 + B \cdot J_1^2 - \eta\sigma_s^2 = 0 \quad (7)$$

with

$$J_1 = tr(\sigma), \quad J'_2 = \frac{1}{2}s_{ij}s_{ij}$$

where  $J'_2$  is the second invariant of deviatoric stress tensor and  $J_1$  is the first invariant of stress tensor.  $s_{ij}$  is the deviator of the stress tensor and  $tr(\cdot)$  represents the trace operator.  $\sigma_s$  is the temperature-dependent yield stress of the dense reference material. The parameter  $\eta$  represents the contribution of geometric hardening as a function of relative density  $\rho_r$ .  $A$  and  $B$  are the parameters of the yield criterion, which are functions of Poisson's ratio  $v$  [16]

$$A = 2(1+v), \quad B = (1-2v)/3 \quad (8)$$

For the uniaxial stress state,  $J_1 = \sigma_{11}$  and  $J'_2 = \sigma_{11}^2/3$ , i.e.,  $A$  and  $B$  should satisfy the following relationship:

$$A/3 + B = 1 \quad (9)$$

The factor  $\eta$  is introduced via the flow stress to characterize geometrical and strain hardening, which is assumed that [17]

$$\eta = (\rho_r^7 - \rho_c^7)/(1 - \rho_c^7) \quad (10)$$

where  $\rho_c$  is an experimental parameter close to the initial relative density, and represents the critical relative density in the state without flow stress for porous material.

The stress increment should follows Hooke's law and can be written as:

$$d\sigma_{ij} = D_{ijkl}^e (d\varepsilon_{kl} - d\varepsilon_{kl}^{vp} - d\varepsilon_{kl}^{th}) \quad (11)$$

where  $D_{ijkl}^e$  is the elastic constitutive tensor,  $d\varepsilon_{kl}$  the total mechanical strain increment,  $d\varepsilon_{kl}^{vp}$  the viscoplastic strain increment, and  $d\varepsilon_{kl}^{th}$  the thermal strain increment.

In this simulation, the elastic modulus  $E$  and Poisson's ratio  $v$  are dependent on temperature and relative density in Eq. 12 [18, 19].

$$E = E_s(T)\rho_r^{3.2}, v = 0.5\rho_r^2 \quad (12)$$

where,  $E_s(T)$  is the elastic modulus of solid material.

The viscoplastic strain increment is calculated on the basis of the viscoplastic theory proposed by Kim and Lee [20]. Assuming that the viscoplastic strain rate  $\dot{\varepsilon}_{ij}^{vp}$  and viscoplastic potential  $\phi$  correspond with the normality rule, the viscoplastic strain rate can be obtained by the flow rule as

$$\dot{\varepsilon}_{ij}^{vp} = \frac{\partial\phi}{\partial\sigma_{ij}} = \frac{\partial\phi}{\partial\sigma_{eq}} \frac{\partial\sigma_{eq}}{\partial\sigma_{ij}} = \frac{\partial\phi}{\partial\sigma_{eq}} \frac{1}{\sigma_{eq}} \left[ \frac{A}{2} s_{ij} + B\sigma_{kk}\delta_{ij} \right] \quad (13)$$

with

$$s_{ij} = \partial J_2'/\partial\sigma_{ij}, \delta_{ij} = \partial J_1/\partial\sigma_{ij} \quad (14)$$

where,  $s_{ij}$  is the deviatoric stress,  $\delta_{ij}$  is the Kronecker delta and  $\sigma_{eq}$  is the effective stress. The relationship between the viscoplastic potential and equivalent stress is expressed in Eq. 15.

$$\frac{\partial\phi}{\partial\sigma_{eq}} = \rho_r \dot{\varepsilon}_{eq}^{vp} \quad (15)$$

where  $\dot{\varepsilon}_{eq}^{vp}$  is the effective viscoplastic strain rate. Substitute Eqs. 15 and 13 can be rewritten as follows:

$$\dot{\varepsilon}_{ij}^{vp} = \frac{\rho_r \dot{\varepsilon}_{eq}^{vp}}{\sigma_{eq}} \left[ \frac{A}{2} s_{ij} + B\sigma_{kk}\delta_{ij} \right] \quad (16)$$

An approximation of Garofalo's hyperbolic sine function of the effective stress and temperature is selected to describe the creep law of the dense material [21], which is given by

$$\dot{\varepsilon}_{eq}^{vp} = \frac{w}{T} [\sinh(\mu\sigma_{eq})]^n \exp\left(-\frac{Q}{\beta T}\right) \quad (17)$$

where,  $w$  is a pre-exponential temperature factor and  $Q$  is the activation energy for the creep deformation process. The parameter  $n$  denotes the strain rate sensitivity.  $\mu$  is a

temperature-independent parameter which prescribes the stress level where the power-law breaks down.  $\beta$  is the universal gas constant.

By combining Eqs. 12, 16 with 17, an modified form of the viscoplastic strain rate for powder material is assumed that:

$$\dot{\varepsilon}_{ij}^{vp} = \frac{w\rho_r}{\sigma_{eq}T} [\sinh(\mu\sigma_{eq})]^n \exp\left(-\frac{Q}{\beta T}\right) \times \left[ \frac{2 + \rho_r^2}{2} s_{ij} + \frac{1 - \rho_r^2}{3} \sigma_{kk} \delta_{ij} \right] \quad (18)$$

In this case, an instantaneous thermal expansion coefficient  $\alpha(T)$  is proposed to define the thermal strain increment with respect to a reference temperature  $T^{ref}$ , which can be written as Eq. 19.

$$d\varepsilon^{th} = \left[ \alpha(T) + \frac{d\alpha(T)}{dT}(T - T^{ref}) \right] dT \quad (19)$$

The evolution of the powder density should follow the mass conservation equation, whereupon it can be written as:

$$\rho_r = \rho_0 \exp(-\varepsilon_v^{vp}) = \rho_0 \exp(-\dot{\varepsilon}_{ij}^{vp} \delta_{ij}) \quad (20)$$

where  $\varepsilon_v^{vp}$  is the cumulative volumetric viscoplastic strain and  $\rho_0$  is the relative density before deformation.

## FEM simulation results

### Model simplification and boundary treatment

This SPS FEM model is treated as an axisymmetric model using the commercial package MSC. Marc. The user subroutines are integrated with the implicit code to simulate the SPS process of metal powders and the corresponding experimental data are presented to verify the simulation.

In the simulation, the initial temperature of the whole SPS apparatus is set to be 25 °C. Two end surfaces of copper electrodes, which are connected with the water-cooling system, are kept constant at 25 °C. The emissivities of the graphite components and silicon-nitride die are assumed to be 0.8. And the position B shown in Fig. 1 is fixed vertically to guarantee the stabilization of the thermocouple. The friction coefficient is set to 0.1 at the contact interfaces.

To simplify the SPS model and avoid additional calculative errors, the mechanical strain is neglected for spacers and electrodes which are modeled with Joule-rigid elements, but not for the sample/punch/die assembly which is modeled with Joule-deformable elements. And the pressure is applied to the top surface of the upper punch as a load boundary. So the axial displacements of the upper spacers

and electrode are maintained consistent with the top surface of the upper punch to keep a durative contact. In reality, the mechanical strains (including the thermal strains) of spacers and electrodes are much smaller than that of the sample/punch/die assembly where the temperature and stress are dominant. The schematic boundary conditions and the corresponding simplification are depicted in Fig. 2.

#### Evolution of electrical potential and temperature distribution

In order to realize the desired heating rate, the imposed voltage drop is taken as a known input variable in the simulation, which is obtained from the on-line recorded profiles.

The measured current and temperature are compared with the simulations in Fig. 3 for different pressures. The simulated current profiles agree well with the experimental results in the middle and late periods, although in the early stage, there are some relatively large departures from the measured profiles. It is mainly because of the complex nonlinear relationship between density and thermoelectric properties of powders in the initial loose state. Surprisingly, the simulated temperature evolutions are nearly consistent with the experimental results for three external pressures. Because a good precision of the thermal–electrical coupling solution is the prerequisite of guaranteeing the precision of the thermal–mechanical coupling solution,

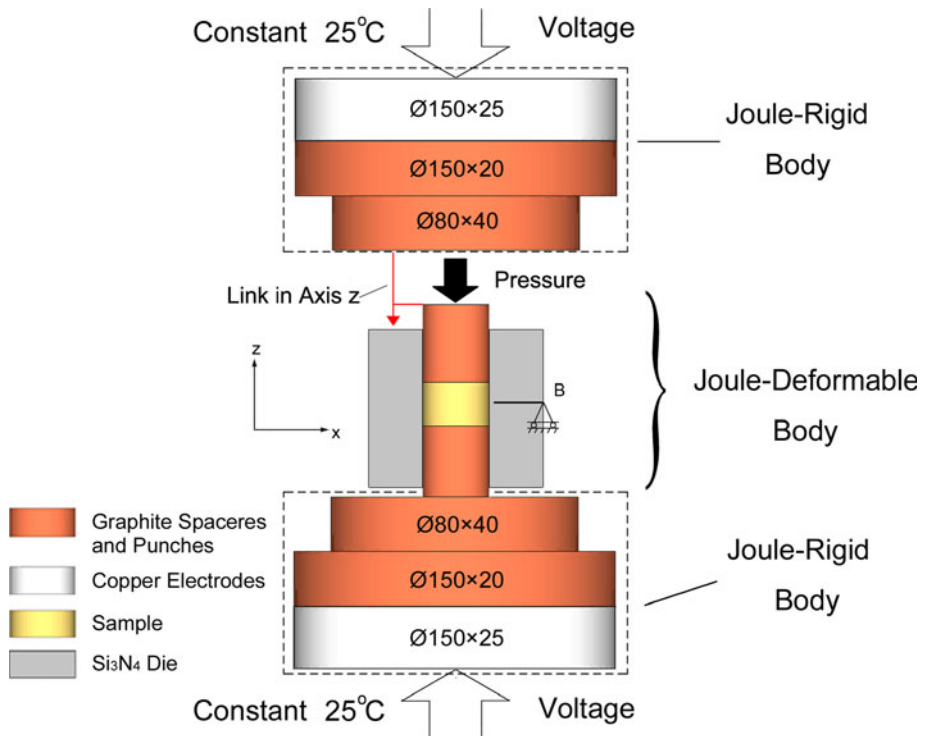
the simulative results of temperature and electrical potential further insure the reliability of this multi-field coupling methodology.

Figure 4 shows the contour plots of temperature distribution within the densification process after 10s, 400s, and 850s for the 60 MPa pressure. It is clearly indicated that at the initial stage of sintering, the temperature at both ends of punches takes the lead to reach the maximum, which is owing to the higher horizontal contact resistances at their smaller contact interfaces with the compact and spacers. At the same time, the majority of the heat generated on these interfaces starts to diffuse axially, and a small amount to the die. Because of the insulating property of the silicon–nitride die, current only flows through the graphite components and powder specimen. Thus, an incipient temperature gradient comes into being.

With the progress of the heating process, the leading role of contact resistances is weakened gradually. The temperature of the specimen increases prominently, and this is due to the cooperation of its own Joule heating generation and the heat conduction from punches. Simultaneously, the spacers and the die absorb a large amount of heat from the hot punches. Thus, the position of the peak temperature is moving toward the interior of powders. At higher temperatures, the heat loss via radiation cannot be neglected anymore, which aggravates the temperature differences in the SPS system during the sintering.

Figure 5 exhibits the temperature gradients along the radius direction in the mid-thickness plane of the specimen

**Fig. 2** Schematic boundary conditions and corresponding simplification illustration for simulation



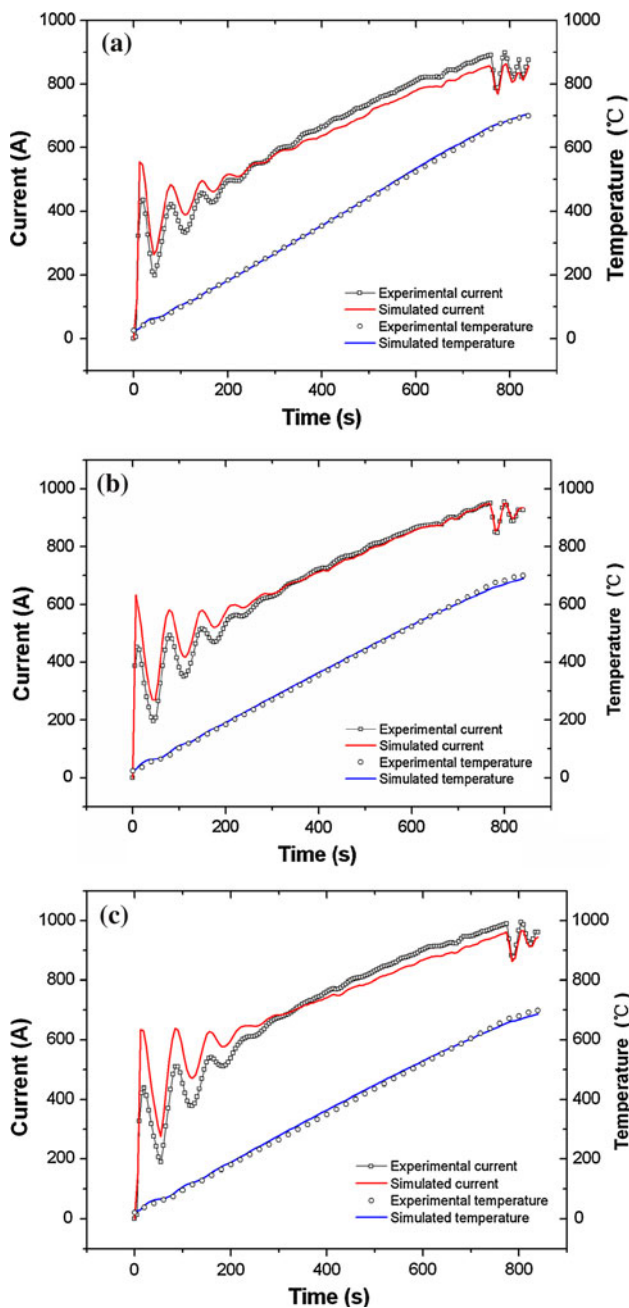


**Fig. 3** Time profiles of electric current and the measured temperature from experiments and simulations under different external pressures for **a** 20 MPa, **b** 40 MPa, and **c** 60 MPa

when the measured temperature reaches 680 °C. The temperature distributions always present a degressive trend along the radius from the center. For the sample/die setup, the silicon–nitride die is responsible for almost all the heat consumption, which makes it a heat sink or a cooler of the sample. The temperature gradient in the sample is always regarded as the prime culprit for the inhomogeneity of material properties and microstructure. In Fig. 5, the maximum temperature difference is decreased from

~40 °C for 20 MPa to ~30 °C for 60 MPa. And because the heat conduction from graphite components is promoted by the increased whole current under the larger pressure, the maximum sintering temperature also declines by ~15 °C. However, the temperature distribution in the die is nearly unchanged for different pressures.

For the decreased temperature gradient under the larger pressure, the deciding factor is the vertical sample/die contact thermal resistance which effectively restrains the temperature gradient along the radius direction especially for 60 MPa, apart from the improved thermal conductivity and electrical conductivity. So the variation laws of contact thermal and electric resistances in the displacement field should get enough emphases.

#### Influence of displacement field on contact resistances

Many studies neglect the influence of the displacement field to simplify the FEM analysis of SPS. That is to say, besides the influence on material thermal–electrical properties, the influence of powder shrinkage on contact thermoelectric effects is unlikely to be considered. Actually, the contact boundaries are changing significantly in the displacement field, which could affect the Joule heat generation at interfaces as well as the heat fluxes through the contact boundaries. The former is resulted from the contact electric resistance, and the latter is controlled by the contact thermal resistance. Therefore, the evolutions of temperature field and electric field are inevitably associated with the displacement field.

Figure 6 reveals the influence of the shrinkage phenomenon on contact boundaries. For convenience of the statement, only the shrinkage  $d$  of powders is mentioned here since it plays a decisive role in the displacement field, although the mechanical strain of the die and punches are also considered in the actual model.

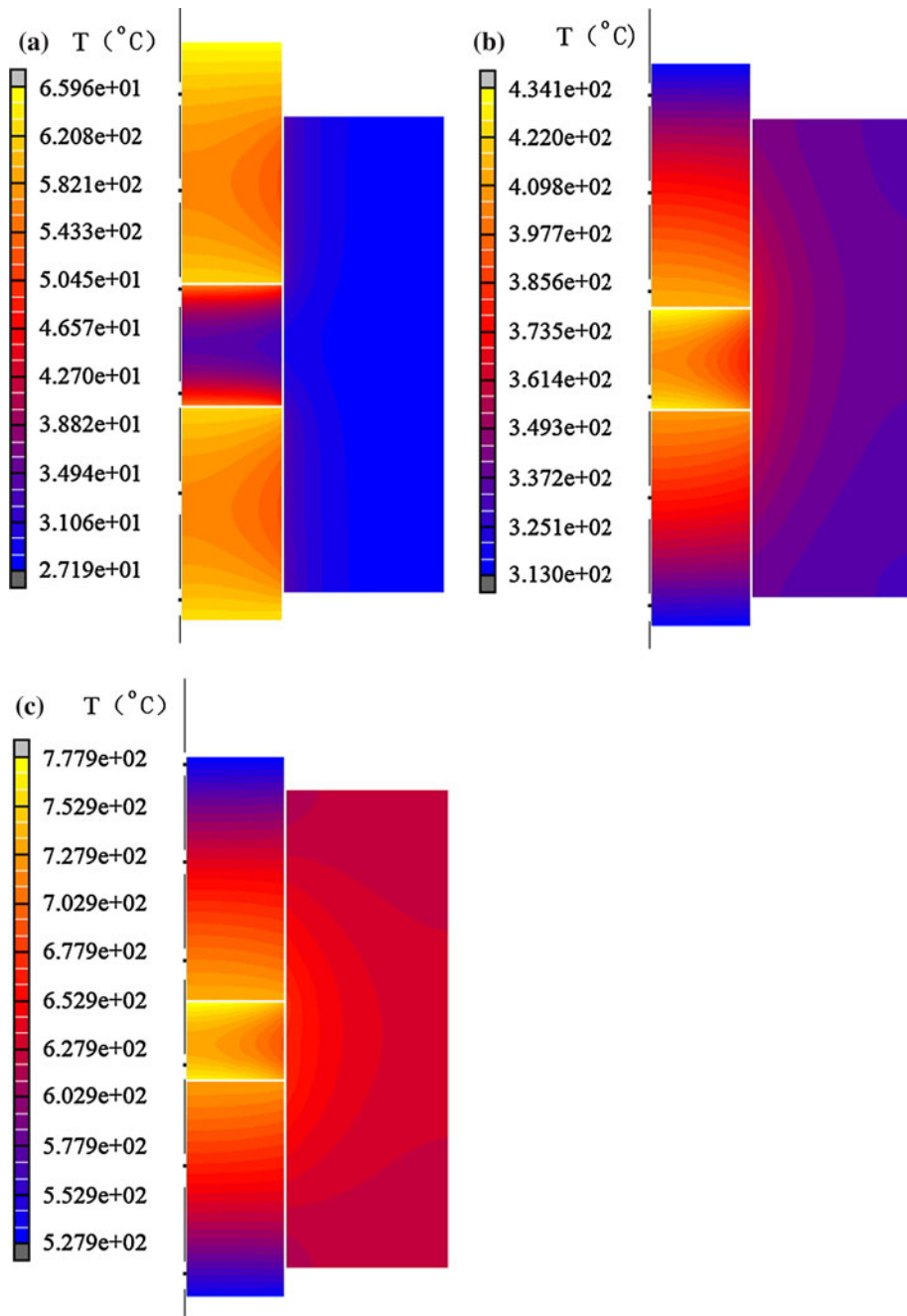
For the exposed surface of the upper punch, heat is transferred only in the form of radiation which is directly proportional to the gradually vanishing surface area during the sintering. The relationship between the shrinkage and the heat radiation of the upper punch can be expressed as:

$$Q_r = e_r A_1 \xi (T_w^4 - T_s^4) (l_1 - d) / l_1 \quad (21)$$

where  $Q_r$  is the heat transfer by radiation,  $e_r$  the emissivity,  $A_1$  the exposed area of the upper punch before compaction,  $\xi$  the Stefan-Boltzmann constant,  $l_1$  the initial height of the corresponding part,  $T_w$  the temperature of the exposed area,  $T_s$  the temperature of the chamber walls.

The theory of the contact resistances is introduced to this model. The localized contact thermal resistance  $\lambda^t$  and contact electrical resistance  $\lambda^e$  in the displacement field can be obtained from Eqs. 22 and 23 [22]:

**Fig. 4** Temperature contour plots under the 60 MPa external pressure for **a**  $t = 10$  s, **b**  $t = 400$  s, **c**  $t = 840$  s



$$\begin{aligned} \lambda_2^e &= \frac{1}{A'_2 \alpha_{e,2}} = \frac{l_2}{A_2(l_2 + d)\alpha_{e,2}}, \quad \lambda_2^t = \frac{1}{A'_2 h_{e,2}} \\ &= \frac{l_2}{A_2(l_2 + d)h_{e,2}} \end{aligned} \quad (22)$$

$$\begin{aligned} \lambda_3^e &= \frac{1}{A'_3 \alpha_{e,3}} = \frac{l_3}{A_3(l_3 - d)\alpha_{e,3}}, \quad \lambda_3^t = \frac{1}{A'_3 h_{e,3}} \\ &= \frac{l_3}{A_3(l_3 - d)h_{e,3}} \end{aligned} \quad (23)$$

where  $A_j$  and  $A'_j$  are areas of the  $j$ th contact interface before and after compaction, and  $l_j$  is the height of the corresponding contact interface before compaction. The

subscript 2 ( $j = 2$ ) represents the interface between the upper punch and the silicon–nitride die, and the subscript 3 ( $j = 3$ ) represents the interface between the specimen and the die. Although  $\lambda_2^e$  and  $\lambda_3^e$  are assumed as the infinite owing to the insulation of the silicon–nitride die, the formulas of  $\lambda_2^t$  and  $\lambda_3^t$  in Eqs. 22 and 23 are still applied in this case.

Equations 22 and 23 show a positive proof of the multi-physics associative function on the thermal–electrical phenomenon of the contact gap. The contact thermal resistances show two completely opposite variation tendencies for these two interfaces. The great change of the

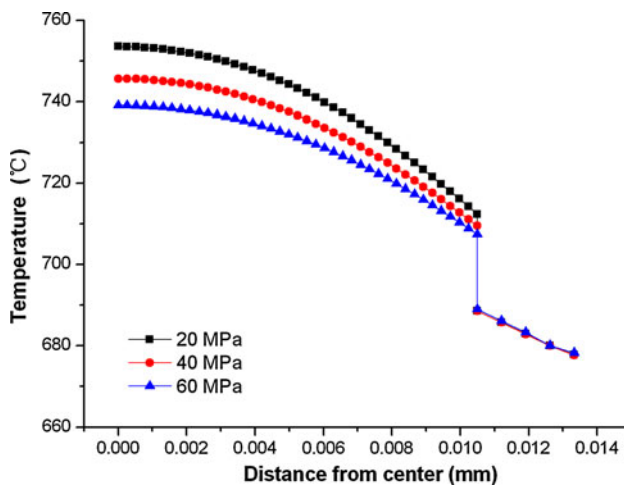


**Fig. 5** Temperature gradients along the radius direction in the mid-thickness plane of specimen for different pressures when the measured temperature reaches 680 °C

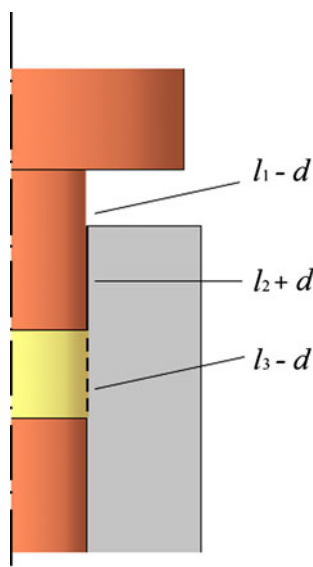


**Fig. 6** SPS contact boundaries affected by the shrinkage phenomenon of powders.  $l_1$ ,  $l_2$ , and  $l_3$  represent the heights of different contact interfaces before compaction.  $d$  represents the shrinkage of powder compact

displacement field causes not only the particular discontinuity in temperature and electrical fields across the contact interfaces, but also the different variation rules of the local thermoelectric effects for different contact pairs.

In Fig. 5, it is obvious that the temperature jump exists at the sample/die interface and will persist throughout the heating process because of the inherent contact thermal resistance, which is noteworthy because the sample/die contact resistance is closely related to the measured temperature by the thermocouple. Figure 5 shows that the temperature gradient commences a descending process with the increase of pressure, because of the larger contact

thermal resistance  $\lambda_3^t$  under the higher axial pressure. In other words, the contact resistance serves as a shield of the compact from the more heat loss under the greater pressure.

Figure 7 reveals the temperature distribution in the axial direction along the inner wall of the die for the 60 MPa pressure. It indicates that such an alterable contact boundary is conducive to build a more authentic temperature gradient. The obvious temperature differences occur at the positions corresponding to the top and bottom surfaces of the specimen because of the horizontal contact resistances between the sample and punches. The temperature symmetry no longer exists, which is contributed to the remolding of the structural geometry. The temperature of the part contacted with the moving punch is slightly higher than that of the part contacted with the fixed punch thanks to the decreasing  $\lambda_2^t$  with the sliding of the moving punch.

#### Density field and stress distribution

The applied external pressure as a crucial control parameter could play the same important role as temperature [23]. The unforeseen stress distribution can lead to the heterogeneous deformation and density distribution. For the pressure-assisted SPS model, the stress and strain are calculated from the aforementioned mechanical constitutive relation of powder material, and the density distribution is derived from the cumulative viscoplastic strain. The varying density is embodied as a varying displacement field on the macroscopic view. In Fig. 8, the recorded displacement field as a critical verification indicator of the thermal–mechanical coupling solution module is compared with the simulation, and a good agreement is displayed.

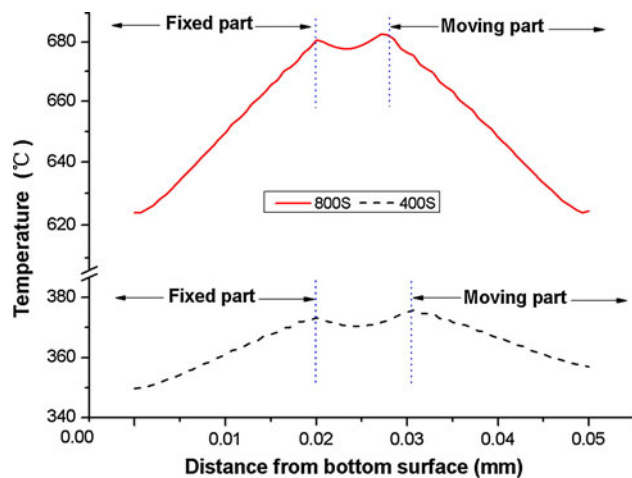


**Fig. 7** Temperature distributions in the axial direction along the inner wall of the die at  $t = 400$  s and 800 s for 60 MPa pressure. The *moving part* represents the part contacted with the moving punch, and the *fixed part* represents the part contacted with the fixed punch

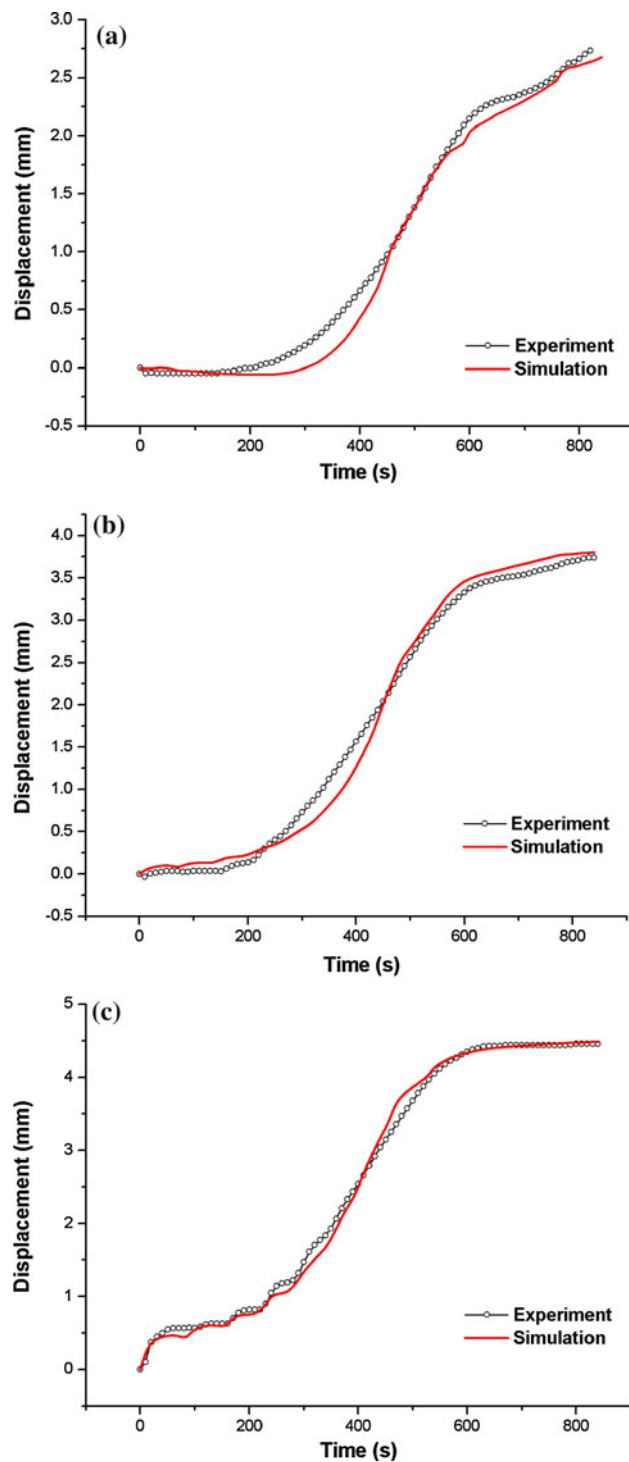
The displacement variations reveal the same slowly growing inclination in the early stage and the later stage of sintering, despite different pressures. In the early stage, the mechanical parameters of powder material changes slightly when the temperature of the sample is lower than about 200 °C. Consequently, powders can achieve an stable equilibrium state in a short time and nearly cease the further densification. When the temperature continues to rise up in the intermediate stage, the yield stress and elastic modulus experience a prominent declining process, which facilitates the explosive growth of the powder shrinkage. However, when entering the later period of sintering, the growth rates all slow down distinctly especially for the 60 MPa because of the higher density close to the dense one.

Figure 9 depicts the stress distributions in the mid-thickness plane of the specimen at the end of sintering. In this case, the axial stress is not dominant anymore. For powders, the radial stress and the angular stress are larger than the axial stress under the 40 and 60 MPa pressures, which cannot happen at room temperature. Figure 9d shows the calculated stress results without thermal expansion for 60 MPa. It can be speculated that the thermal strain owing to the thermal expansion of the die and the compact alters the stress distributions remarkably. When the external pressure is raised from 20 to 60 MPa, the radial and angular stress increase tremendously along with the improvement of the densification level. However, the axial stress is basically consistent with the steady-state outer load. Actually, the prominent growth of the radial stress and the angular stress of powders also helps to improve the material homogeneity.

The distribution of relative density at the end of sintering is shown in Fig. 10. For the 20 MPa external pressure, the distribution of relative density presents an obvious degression trend along the radial direction. By contrast, the relative density distribution in Fig. 10a behaves many similarities with the temperature distribution within the sample in Fig. 4. Because the temperature distributions under different pressures share almost the same tendency, it is logical to presume that under the lower pressure, the density distribution is very susceptible to the temperature field and the control role of stress is not outstanding compared with the one under the higher pressure. For 40 and 60 MPa, the density span decreases and a large area of the low-density districts at the edge gets a very good improvement. So the comprehensive effect of the interior stress promotes the densification of the low-temperature positions.

## Discussion

The purpose of this article is to discuss a numerical methodology and a FEM model available for the single-step



**Fig. 8** Simulated and measured time profiles of displacement for **a** 20 MPa, **b** 40 MPa, and **c** 60 MPa

SPS processing technique rather than to analyze the process parameters from the perspective of material properties. A large temperature gradient is created artificially by using the silicon–nitride die in order to investigate the influences of the densification process and stress on the

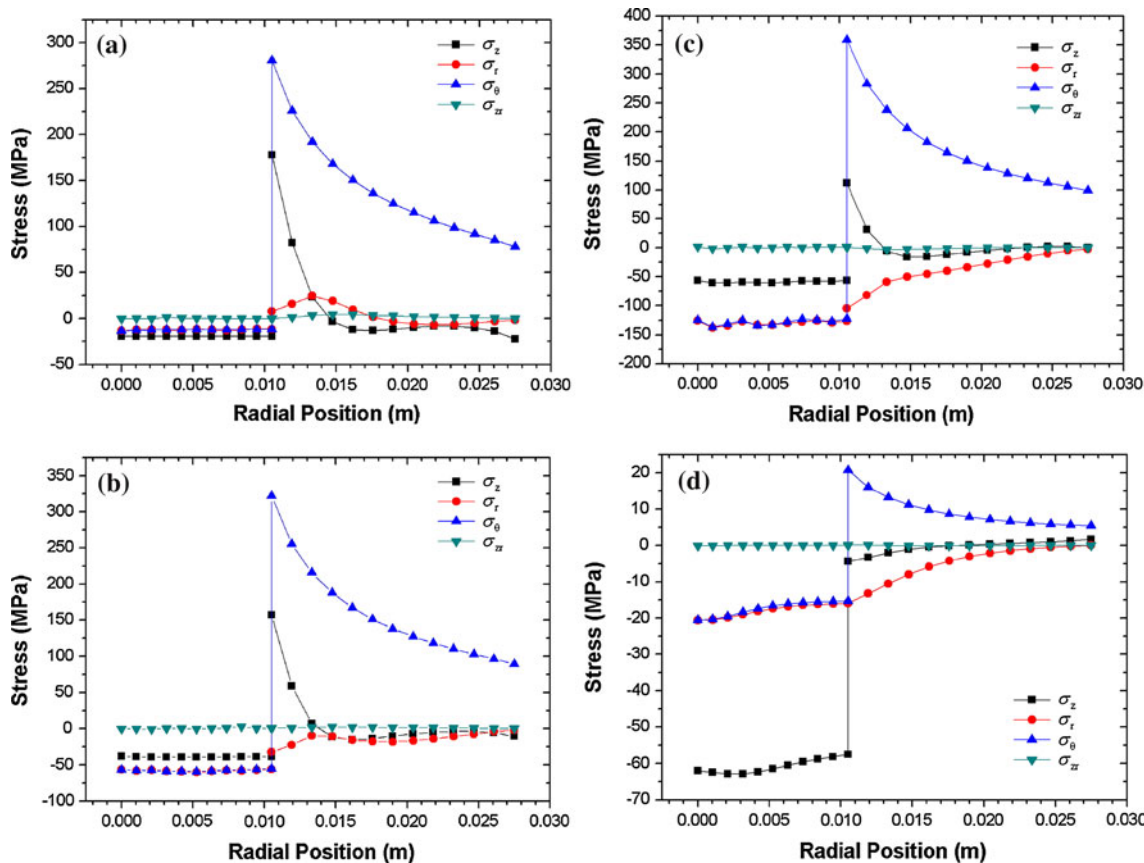


**Fig. 9** Stress distributions along the radius direction in the mid-thickness plane of specimen with thermal expansion for **a** 20 MPa, **b** 40 MPa, and **c** 60 MPa, and without thermal expansion for **d** 60 MPa

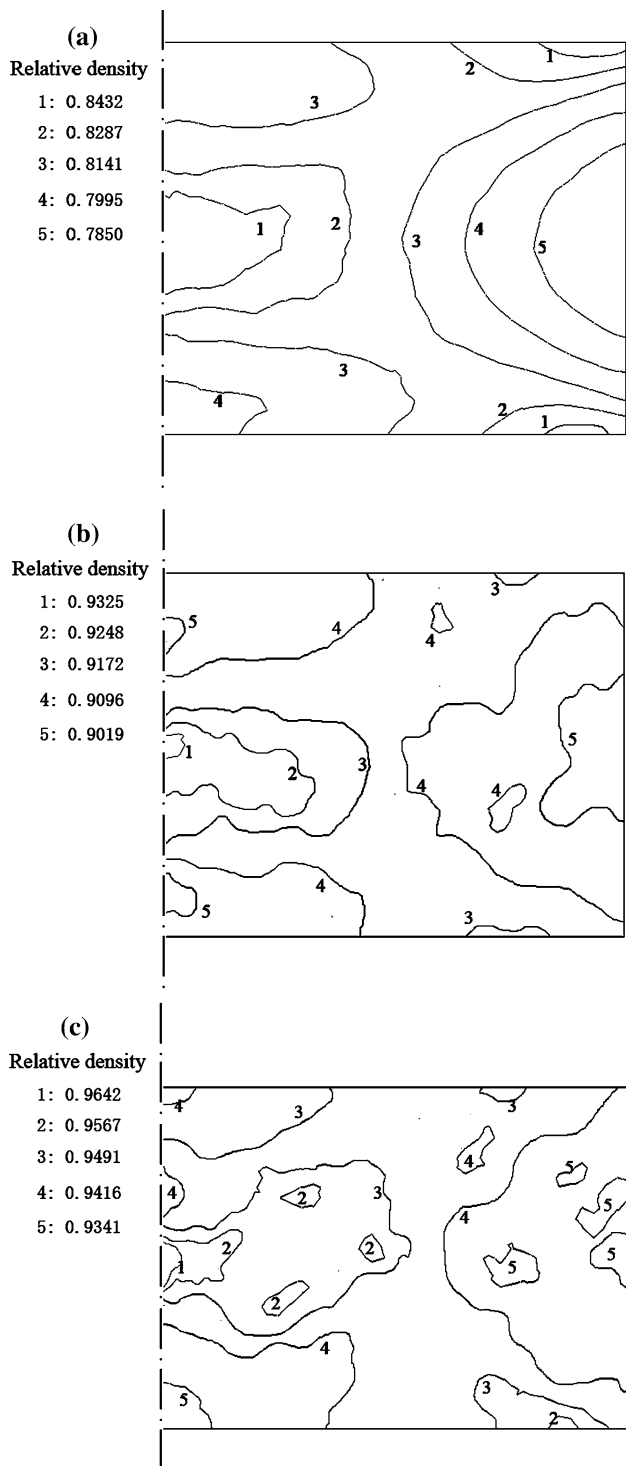
inhomogeneous temperature distribution more intuitively. As described in Fig. 5, for the pressure-assisted SPS process, a suitable pressure can dramatically decrease the unfavorable temperature gradient and compensate for the densification of the colder regions. This cannot be interpreted by the SPS FEM models which neglect the function of the external load and only focus on temperature and electrical fields.

Figure 11 depicts the measured hardness profiles along the radius direction on the mid-thickness cross section for different external pressures. For 20 MPa, the hardness at the brim is remarkably lower than the center hardness. But the hardness distribution tends to be more uniform with the increase of pressure, which is consistent with the distribution rule of the relative density. Thus, the material inhomogeneity described in Fig. 10 can be confirmed by the hardness distribution. By Archimedes' method, the measured whole mean relative density is 0.843, 0.935, and 0.966 for 20, 40, and 60 MPa, respectively, which are all slightly larger than the simulated data. So the multi-field coupled model still needs to be improved.

The effect of the variational local thermoelectric properties of powder material on temperature field and electrical

field is investigated in this article, which is of theoretical value and practical significance. Because a large amount of Joule heat could be generated locally in the high-density regions, these denser locations would firstly realize sintering and leave the low-density regions insufficiently sintered, which would make the temperature field and electrical field highly dependent on the variation of the local density. Some SPS experimental observations of conductive powders indicate that the current localization along the paths of the least resistance can result in the local Joule heat to be high enough to melt the conductive material, and some “channels” of the sintered material would be created [10]. In addition, if the applied load is not big enough, the heterogeneity inside the specimen could generate the difference in shrinkage and the resulting distortion phenomenon.

As mentioned before, many simulations treat the powder compact as the isotropic elastic solid. Some [9] interpret the rationality of this simplification and consider that a large portion of the sintering process occurs at the phase approaching to the solid and the further densification relies on the diffusion along grain boundaries and/or through the lattice in the later period. However, powders are always energized in a low density and sintered in a single-step



**Fig. 10** Distribution contours of relative density at the end of sintering for **a** 20 MPa, **b** 40 MPa, and **c** 60 MPa

process, thus the inhomogeneous density distribution has been produced from the beginning and will exist over an extended period. This is clearly different from the homogeneous solid material. Moreover, when the relative

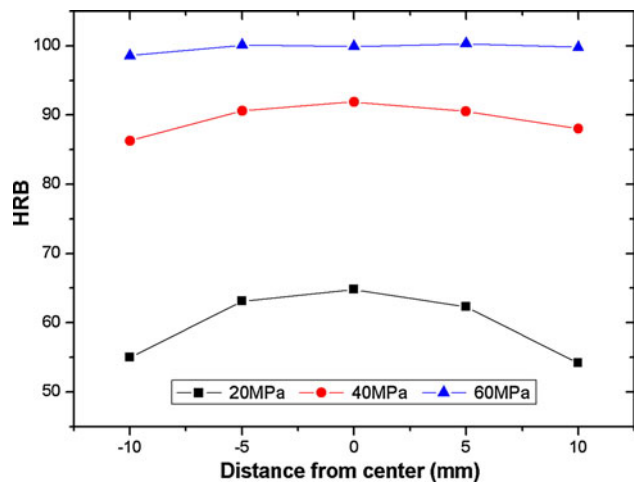


**Fig. 11** Measured hardness profiles along the radius direction on the mid-thickness cross section for different external pressures

density is greater than 0.9, even though there are only the isolated pores left, the further densification is also driven by yielding and creep [24]. Therefore, the consideration of the powder model has a positive significance on the understanding of the SPS mechanism and the optimization of processes for the more complex parts.

## Conclusion

In this study, a coupled thermal–electric–mechanical FEM procedure which consists of a thermal–electrical coupling solution modulus and a thermal–mechanical coupling user-subroutines solution modulus, is presented for the one-step-forming SPS process of powder material. This developed FEM model gives concern about the influence of the local density on material properties, as well as the effect of the displacement field on contact boundaries. Therefore, the external pressure not only elevates the driving force of densification, but also greatly affects the temperature field and electrical field by means of modifying the geometry structure and the contact thermal and electric resistances.

The simulation shows that the sintering temperature and the temperature gradient are decreased by increasing the external pressure from 20 to 60 MPa. The vertical sample/die contact thermal resistance effectively restrains the temperature gradient along the radius direction especially under the higher pressure. The distributions of stress show that the thermal expansion of the die and powder compact affects the stress distributions remarkably. And the comprehensive effect of stress compensates for the densification of the colder regions. The experiments demonstrate the reliability of the adopted constitutive model of powder material, and illustrate that the interrelationship between the temperature gradient and the intrinsic stress distribution

plays a paramount role in the densification mechanism of the SPS powders.

**Acknowledgements** This study was supported by the National Natural Science Foundation of China (Grant no. 50325516) and the Fundamental Research Funds for the Central Universities, SCUT (Grant no. 2009ZM0040).

## Appendix

### Iron properties

$$\begin{aligned}\rho(\text{kg m}^{-3}) &= 7880 \\ E_s(T)(\text{GPa}) &= 1.96 \times 10^2 (1 - 2.1 \times 10^{-4}(T - 298) \\ &\quad - 1.7 \times 10^{-7}(T - 298)^2 \\ &\quad - 3.2 \times 10^{-10}(T - 298)^3) \\ \alpha(T)(1/\text{K}) &= (4.994 + 0.030T - 2.696 \times 10^{-5}T^2 \\ &\quad + 8.390 \times 10^{-9}T^3) \times 10^{-6} \\ K_s(T)(\text{W}/(\text{m K})) &= 73.014 - 5.0 \times 10^{-2}(T - 273) \\ &\quad - 7.096 \times 10^{-5}(T - 273)^2 \\ &\quad + 1.366 \times 10^{-7}(T - 273)^3 \\ &\quad - 5.323 \times 10^{-11}(T - 273)^4 \\ R_s(T)(1/(\Omega \text{ m})) &= (0.096 + 2.139 \times 10^{-4}(T - 273) \\ &\quad + 2.240 \times 10^{-6}(T - 273)^2 - 1.803 \\ &\quad \times 10^{-9}(T - 273)^3 \\ &\quad + 3.571 \times 10^{-13}(T - 273)^4)^{-1} \times 10^6 \\ c_p(T)(\text{J}/(\text{kg K})) &= 317.202 + 0.433 \times T\end{aligned}$$

### Graphite properties

$$\begin{aligned}\rho(\text{kg m}^{-3}) &= 1850 \\ E(\text{GPa}) &= 200 \\ \alpha(T)(1/\text{K}) &= 8 \times 10^{-6} \\ K(T)(\text{W}/(\text{m K})) &= 65 - 1.7 \times 10^{-2}T \\ R(T)(1/(\Omega \text{ m})) &= (26 - 3 \times 10^{-2}T + 2 \times 10^{-5}T^2 \\ &\quad - 6.4 \times 10^{-9}T^3 + 7.8 \times 10^{-13}T^4)^{-1} \times 10^6 [23] \\ c_p(T)(\text{J}/(\text{kg K})) &= 310.5 + 1.7 \times T\end{aligned}$$

### Silicon–nitride properties

$$\begin{aligned}\rho(\text{kg m}^{-3}) &= 3184 \\ E(\text{GPa}) &= 330 \\ \alpha(T)(1/\text{K}) &= 2.7 \times 10^{-6}(0.856 + 4.919 \times 10^{-4}T) \\ K(T)(\text{W}/(\text{m K})) &= 34.271 - 0.0141 \times T \\ c_p(T)(\text{J}/(\text{kg K})) &= 740\end{aligned}$$

### Copper properties [9]

$$\begin{aligned}\rho(\text{kg m}^{-3}) &= 7850 \\ K(T)(\text{W}/(\text{m K})) &= 420.66 + 0.07 \times T \\ R(T)(1/(\Omega \text{ m})) &= (5.5 + 0.038 \times T)^{-1} \times 10^9 \\ c_p(T)(\text{J}/(\text{kg K})) &= 355.3 + 0.1 \times T\end{aligned}$$

## References

1. Langer J, Hoffmann MJ, Guillon O (2009) Acta Mater 57:5454
2. Zavaliongos A, Zhang J, Krammer M, Groza JR (2004) Mater Sci Eng A 379:218. doi:[10.1016/j.msea.2004.01.052](https://doi.org/10.1016/j.msea.2004.01.052)
3. Tiwari D, Basu B, Biswas K (2009) Ceramics Int 35:699. doi:[10.1016/j.ceramint.2008.02.013](https://doi.org/10.1016/j.ceramint.2008.02.013)
4. Maizza G, Grasso S, Sakka Y (2009) J Mater Sci 44:1219. doi:[10.1007/s10853-008-3179-8](https://doi.org/10.1007/s10853-008-3179-8)
5. Yang J, Li Y, Li X, Guo L, Chen W (2007) Special Cast Non-ferrous Alloy 27:24 In Chinese
6. Liu X-M, Song X-Y, Zhang J-X, Zhao S-X, Wei J (2008) Chinese J Nonferrous Metal 18:221 In Chinese
7. Hulbert DM, Jiang D, Anselmi-Tamburini U, Unuvar C, Mukherjee AK (2008) Mater Sci Eng A 488:333. doi:[10.1016/j.msea.2007.11.054](https://doi.org/10.1016/j.msea.2007.11.054)
8. Vanmeensel K, Laptev A, Van der Biest O, Vleugels J (2007) J Euro Ceramic Soc 27:979. doi:[10.1016/j.jeurceramsoc.2006.04.142](https://doi.org/10.1016/j.jeurceramsoc.2006.04.142)
9. Wang X, Casolco SR, Xu G, Garay JE (2007) Acta Mater 55:3611
10. McWilliams B, Zavaliongos A (2008) J Mater Sci 43:5031. doi:[10.1007/s10853-008-2744-5](https://doi.org/10.1007/s10853-008-2744-5)
11. Grasso S, Sakka Y, Maizza G, Hu C (2009) J Am Ceram Soc 92:2418
12. Matsugi K, Kuramoto H, Yanagisawa O, Kiritani M (2003) Mater Sci Eng A 354:234. doi:[10.1016/s0921-5093\(03\)00012-1](https://doi.org/10.1016/s0921-5093(03)00012-1)
13. Anselmi-Tamburini U, Gennari S, Garay JE, Munir ZA (2005) Mater Sci Eng A 394:139. doi:[10.1016/j.msea.2004.11.019](https://doi.org/10.1016/j.msea.2004.11.019)
14. Wang D, Wu Y, Jiao M, Yu J, Xie T, Yin Y (2008) Powder Metall Technol 26:88 In Chinese
15. Montes JM, Cuevas FG, Cintas J (2007) Metall Mater Trans B Proc Metall Mater Proc Sci 38:957
16. Doraivelu SM, Gegel HL, Gunasekera JS, Malas JC, Morgan JT, Thomas JF Jr (1984) Int J Mech Sci 26:527. doi:[10.1016/0020-7403\(84\)90006-7](https://doi.org/10.1016/0020-7403(84)90006-7)
17. Li Y-Y, Zhao W-B, Zhou Z-Y, Chen P-Q (2006) Trans Nonferrous Metal Soc China (English Edition) 16:311
18. Li Y-y, Chen P-q, Xia W, Zhou Z-y, Li W-f (2006) Trans Nonferrous Metal Soc China 16:507. doi:[10.1016/s1003-6326\(06\)60088-5](https://doi.org/10.1016/s1003-6326(06)60088-5)
19. Song Y, Li Y-Y, Zhou Z-Y, Zheng Z-X, Chen P-Q (2010) Trans Nonferrous Metals Soc China (English Edition) 20:1470
20. Kim HS, Lee DN (1999) Mater Sci Eng A 271:424. doi:[10.1016/s0921-5093\(99\)00279-8](https://doi.org/10.1016/s0921-5093(99)00279-8)
21. Wikman B, Svoboda A, Hagglad HA (2000) Comput Method Appl Mech Eng 189:901
22. Zhang J, Zavaliongos A, Kraemer M, Groza J (2002) In: Proceedings of a symposium on modelling the performance of engineering structural materials III, Minerals, Metals and Materials Society, Columbus
23. Wang C, Cheng L, Zhao Z (2010) Comput Mater Sci 49:351. doi:[10.1016/j.commatsci.2010.05.021](https://doi.org/10.1016/j.commatsci.2010.05.021)
24. Conway JJ, Nettleship I, McAfee RJ, Loehlein ES (2002) In: Advance in powder metallurgy and particulate materials 2002, vol 9. (published by MPIF)